Cu-doping Increases Capacity Retention in

 $LiNi_{0.6}Mn_{0.2}Co_{0.2}O_2$  (NMC622) by Altering the

Potential of the Ni-based Redox Couple and

**Inhibiting Particle Pulverization** 

Christopher P. Woodley, Rachel A. Cooper, Bart M. Bartlett\*

Department of Chemistry, University of Michigan, 930 N. University Avenue, Ann Arbor, MI

48109-1055 USA

Corresponding author e-mail address: bartmb@umich.edu

**Abstract** 

To discern the influence of Cu<sup>2+</sup> as a dopant on both the structural and electrochemical

characteristics of LiNi<sub>0.6</sub>Mn<sub>0.2</sub>Co<sub>0.2</sub>O<sub>2</sub> (NMC622), Cu<sup>2+</sup>(aq) was added to the co-precipitation

synthesis from the constituent ions. At 5 mol-% Cu<sup>2+</sup>, a single-phase Cu-NMC product results,

evidenced by an increase in d-spacing along the [003] and [104] directions and a slight increase in

the crystal volume of the *R*–3*m* hexagonal (rock-salt superstructure) lattice. XRD data and high-resolution TEM imaging support Cu<sup>2+</sup> doping on the transition metal 3b Wyckoff sites. Galvanostatic cycling of Cu-NMC shows a reversible gravimetric capacity of 102 mAh/g compared to 136 mAh/g for undoped NMC. Despite the lower capacity, the discharge capacity retention of Cu-NMC is 89% after 100 cycles, compared to only 70% for NMC. XPS analysis reveals that this lower capacity is due to an increase in the concentration of Ni<sup>3+</sup> ions at the surface, while XRD data collected at the top and bottom of charge show a smaller decrease in crystalline domain size for Cu-NMC (40.5% decrease) compared to NMC (74.7% decrease), translating to pulverization of the secondary particles.

KEYWORDS: lithium-ion battery cathode, cation doping, NMC622 capacity retention, surface oxidation, post-cycling characterization

#### Introduction

The adoption of electric vehicles (EVs) has increased drastically, and this demand is expected to exponentially increase over the next two decades. The most common cathode active material used in today's EVs is  $\text{LiNi}_x \text{Mn}_y \text{Co}_z \text{O}_2$  (x + y + z = 1, NMC). NMC has many benefits including long cycle life (100 reversible cycles with 94.6% capacity retention cycled from 3.0 V to 4.3 V vs.  $\text{Li}^{+/0}$ ), large potential window (3.0 V – 4.3 V vs.  $\text{Li}^{+/0}$ ), high observed specific capacity (200 mAh/g at 4.6 V when coupled with a graphite anode, with a theoretical capacity of 268 mAh/g, assuming 1 mole of electrons is donated), power density of 100 – 650 W/Kg, and safety. The primary

electrochemically active ions are formally Ni<sup>2+</sup>, Ni<sup>3+</sup>, and Ni<sup>4+</sup>, which couple to Li<sup>+</sup> extraction/insertion from NMC during charging/discharging, respectively. <sup>13</sup> However, NMC does have an issue with capacity loss due to irreversible structural rearrangement to a spinel phase that is expedited at the top of charge (potentials greater than or equal to 4.3 V vs. Li<sup>+/0</sup>). <sup>14,15</sup> The addition of dopants have been shown to improve capacity retention and overall cycle life. For example, when silicon as Si<sup>4+</sup> is added in a co-precipitation synthesis, the doped material shows a 10% increase in capacity and lower resistance at the SEI interface and charge-transfer resistance, but there is still a significant capacity fade. <sup>16</sup> Upon adding Mg<sup>2+</sup> and Al<sup>3+</sup>, there is a drop in capacity due to anti-site defects. <sup>17</sup> In work to make zero-strain cathodes, Zhang *et al.* have used co-precipitation to replace cobalt with high entropy mixtures of Ti, Mg, Nb, Al, and Zr ions, and the resulting cells show a significant increase in capacity retention, with cycle life of 85% after 1,000 cycles in coin cells using a Li-metal anode. <sup>18</sup> This improvement is thought to arise as cobalt is replaced with redox inactive metal ions that reduce the total irreversible volume change.

In this manuscript, we focus on adding Cu<sup>2+</sup> to the NMC structure. The hypothesis is that Cu<sup>2+</sup> is Jahn-Teller distortive, which could minimize strain upon cycling. In layered materials for sodium-ion batteries, adding Cu<sup>2+</sup> gives rise to 55% capacity retention after 100 cycles, compared to only 31% capacity retention in the undoped material. In this case, the Cu<sup>2+</sup> inhibits the phase transition from P2-O2 to P2-O4, which has lower volume expansion. <sup>19,20</sup> Adding Cu<sup>2+</sup> to sodiumion battery cathode materials also decreases the capacity by 17% as Cu<sup>2+</sup> ions replace the Ni-ions, thereby reducing the amount of Na<sup>+</sup> that can be reversibly extracted. <sup>21,22</sup> In addition to this testable

hypothesis for NMC, we selected Cu<sup>2+</sup> for a practical reason. To recycle batteries by hydrometallurgy at the end of their usable lives, they are shredded, and Cu<sup>2+</sup> can be leached from the Cu-foil current collector into solution. <sup>23-25</sup> One benefit of adding copper is that its addition shows a decrease in capacity fade during cycling by changing the surface and particle size of the NMC, although there remains the tradeoff of a decreased discharge capacity. <sup>26-28</sup> The exact mechanism for the decrease in discharge capacity and increase in capacity retention has yet to be thoroughly understood in the Li-case. In this work, we show an increase in the Ni oxidation state at the surface, which makes the electrochemical oxidation and reduction of Ni less reversible. Moreover, adding Cu<sup>2+</sup> gives rise to a smaller crystalline domain size in the synthesized material. Consequently, there is a smaller propensity for particle fracture when the material is oxidized (charged) and reduced (discharged).

## **Experimental Section**

# **Experimental Synthesis**

NMC materials were synthesized by a co-precipitation method. In a typical reaction, 0.6 moles nickel (II) sulfate hexahydrate (Acros Organics), 0.2 moles manganese (II) sulfate monohydrate (Thermo Scientific), and 0.2 moles cobalt (II) sulfate heptahydrate (Alfa Aesar) were dissolved in 100 mL Milli-Q water (18.2 M $\Omega$ -cm) with vigorous stirring for 30 min. The pH of the solution was adjusted to 11 using 3 M ammonium hydroxide (Fisher Chemical), while stirring was continued for 30 min to give a dark brownish-green suspension. Then 2 M oxalic acid (Alfa Aesar)

was added to adjust the pH to 2, and the solution was stirred for another 2 h, giving rise to a whiteish-gray colored suspension. For samples doped with copper, either 0.05 moles or 0.1 moles of copper (II) sulfate pentahydrate (Fisher Scientific) were added to the starting aqueous mixture. This suspension was vacuum filtered and dried overnight at 120°C. The dried precursor was then ground down by mortar and pestle. The fine powder obtained was further ground by mortar and pestle with 1.05 moles anhydrous lithium hydroxide (Sigma-Aldrich) and subsequently annealed at 860 °C for 12 h with a 2 °C/min ramp rate to make the final cathode active material (CAM). The typical isolated reaction yield is 3.22 g, 74.5% based on the Ni<sub>0.6</sub>Mn<sub>0.2</sub>Co<sub>0.2</sub>(OH)<sub>2</sub>. The annealed material was again pulverized by mortar and pestle prior to making electrodes.

## **Electrode Preparation**

The binder was made by adding 8 wt-% Solef 5130 poly (vinylidene fluoride) (PVDF) to *N*-methylpyrolidinone (NMP) in an N<sub>2</sub>-filled-glovebox. Then, a planetary mixer (THINKY AR-100 Conditioning Mixer) was used until PVDF was completely dispersed. In a nitrogen-filled glovebox, a 96:2:2 ratio mixture of CAM / carbon / binder was made and dispersed in NMP to make a 50 wt-% dispersion. Specifically, Timcal Super P Li carbon was combined with the binder to make a carbon dispersion and half the NMP was added along with five 5 mm zirconia milling beads, which was then mixed by hand with a glass pipette. Then, a THINKY mixer was used to disperse the carbon by mixing over 5 min in 1 min intervals at 2000 rpm. Next, the CAM and the remaining half of NMP were added. Then, hand mixing and THINKY mixing were performed again, with the latter for another 5 min in 1 min intervals at 2000 rpm. This slurry was coated on

battery grade Al foil (All Foils) with a 6-mil drawdown bar (BYK Instruments) and dried for 5 min at 120 °C in an oven. <sup>29,30</sup> After drying, the cathode was pressed to 30% porosity using a lab roll press (Tob New Energy Technology Lab Roll Press Machine TOB-SG-100).

# **Battery Assembly**

A 10 mm diameter punch of the cathode was punched, and vacuum dried overnight at 60 °C before being brought into an argon-filled glovebox. 2032-size 316 stainless steel coin-cell parts from Pred Materials were used for battery assembly. In an argon-filled glovebox, half-cell (Li metal combined anode and reference electrode) coin cells were assembled. First, the cathode was placed in the coin-cell cap, followed by the addition of 37.5 μL 1 M LiPF<sub>6</sub> in a 50/50 v/v ratio of ethylene carbonate and dimethyl carbonate electrolyte (Sigma-Aldrich). Next, an ENTEK 18 mm diameter × 12 μm thick separator was placed on top of the electrolyte and cathode. A plastic gasket was placed down, followed by the addition of 37.5 μL electrolyte. A 16 mm diameter × 0.06 mm thick punch of polished lithium metal from MSE supplies was placed next, followed by a 15.5 mm diameter × 0.5 mm thick spacer and a wave spring. Finally, the coin cell was capped with the base. Once the coin cells were assembled, they were crimped shut at 0.8 T using an electric crimper (MTI digital pressure controlled electric crimper MSK-160E).

# **Electrochemical Testing**

Cyclic voltammetry (CV) was performed with a CH Instrument 1000A potentiostat at a 0.1 mV/s scan rate over a potential window of 3.0 to 4.3 V vs Li<sup>+/0</sup>. All potentials in the remainder of this

manuscript are referenced vs. Li<sup>+/0</sup>. A Metrohm Autolab electrochemical station with current calculated for a 1 *C* charge was used for the chronopotentiometry (CP). Electrochemical impedance spectroscopy (EIS) measurements were conducted using a 10-mV amplitude and a frequency range of 100 KHz to 1 Hz on a Solarton ModuLab Impedance Analyzer. The collected data was then modeled using ZView software.<sup>31</sup> CV, CP, and EIS tests were carried out with assembled half-cell coin-cells. Battery testing by CP was performed on a Neware battery cycler. One hundred total cycles, (three charge / discharge cycles of 0.1 *C* from 3.0 to 4.3 V for formation followed by ninety-seven 1 *C* charge / discharge cycles from 3.0 to 4.3 V) were used for cycle-life testing. Rate capability was tested using 3 cycles each at of 0.1 *C*, 0.2 *C*, 0.3 *C*, 0.5 *C*, 1 *C*, 3 *C*, and 6 *C*, followed by one final 0.1 *C* cycle. The current for all *C*-rates was calculated using 175 mAh/g as the reversible capacity.

# **Materials Characterization**

X-ray diffraction (XRD) was measured on a Panalytical Empyrean diffractometer at a power of 1.8 kW (45 kV, 40 mA) with Cu K $\alpha$  ( $\lambda$  = 1.5418 Å) radiation using a zero-background holder made of single crystal silicon. The detector was an X'Celerator Scientific, a position-sensitive 1D detector equipped with Bragg–Brentano HD X-ray optic delivering only K $\alpha$  radiation. Patterns were collected with a sampling step of 0.0084 and a scan rate of 0.018°·s<sup>-1</sup> from 5 – 80° 2θ. All peak areas and all planes were calculated in the lithium nickel manganese cobalt oxide (NMC) powder using Jade software<sup>32</sup> and the lattice parameters for the *R-3m* space group.<sup>33</sup> GSAS-II<sup>34</sup>

with an instrument parameter file created using NIST SRM 660c (LaB<sub>6</sub>)<sup>35</sup> was used for X-ray diffraction data Rietveld refinement<sup>36</sup> and VESTA<sup>37</sup> was used to create structural models. Highangle annular dark-field scanning transmission electron microscopy (HAADF-STEM) was performed on a Thermo Fisher Scientific Spectra 300 probe-corrected STEM operated at 300 kV and the HAADF images were collected in a range of 62–200 mrad with a convergence angle of 22 mrad and analyzed using Gatan. The TEM sample was prepared using a Thermo Fisher Scientific Helios G4 UXe focus ion beam (FIB). X-ray photoelectron spectroscopy (XPS) was collected on a Kratos Axis Ultra using a monochromatic Al source at a pass energy of 20 eV with emission of 10 mA and anode HT of 14 kV. The spectra were corrected for charging by referencing the C(1s) peak to 284.8 eV. All peaks were fitted in Casa XPS<sup>38</sup> with the Shirley-type background. X-ray fluorescence spectroscopy (XRF) for elemental analysis was measured with a Thermo Scientific ARL QUANT'X using a KitachiSDD detector using a Cu K-α source under vacuum. Scanning electron microscopy (SEM) was done on a JEOL-7800FLV FE SEM coupled with an energydispersive X-ray spectrometry (EDX) operated on an Oxford XMaxN 80mm<sup>2</sup> silicon-drift energydispersive X-ray spectrometer using Oxford Aztec v3.3 EDX acquisition and processing software for analysis.

#### **Results and Discussion**

Synthesis, Structure, and Composition. NMC compounds were prepared in two steps: (equation1) precipitating a hydroxide precursor containing the transition metal (TM) cations in the desired

stoichiometric ratio using soluble sulfate salts, and (**equation 2**) calcining in air with lithiation. The details of the precursor synthesis have been recently reviewed,<sup>39</sup> and the balanced equations for preparing NMC are:

$$0.6 \text{ Ni}^{2+}(aq) + 0.2 \text{ Mn}^{2+}(aq) + 0.2 \text{ Co}^{2+}(aq) + 2\text{OH}^{-}(aq) \rightarrow \text{Ni}_{0.6}\text{Mn}_{0.2}\text{Co}_{0.2}(\text{OH})_2(s)$$
 (1)

$$Ni_{0.6}Mn_{0.2}Co_{0.2}(OH)_2(s) + LiOH(s) + \frac{1}{2}O_2(g) \rightarrow LiNi_{0.6}Mn_{0.2}Co_{0.2}O_2(s) + \frac{3}{2}H_2O(g)$$
 (2)

For the doped material, we add  $Cu^{2+}(aq)$  directly to the precipitation reaction in equation 1 (as  $CuSO_4$ ). This material is referred to as Cu-NMC throughout the remainder of the manuscript.

The XRD patterns in **Figure 1** show that when 5 mol-% Cu<sup>2+</sup> is added to the TM precursor mixture, no additional Bragg reflections appear in the final product. As an internal standard for assigning peak positions, we rely a Si standard of SRM 640e.<sup>40</sup> However, there are increases of 0.004 Å and 0.0003 Å in the *d*-spacing for the (003) and (104) planes, respectively. These planes are illustrated in **Figure S1**, and the increases hint that Cu<sup>2+</sup> substitutes for the TM ions on the 3b Wyckoff sites. As prepared, the TM ions are present formally as Mn<sup>4+</sup>, Co<sup>3+</sup>, and Ni is mixed valent between Ni<sup>2+</sup> and Ni<sup>3+</sup> in NMC622.<sup>41</sup> We note that Ni<sup>3+</sup> and the added Cu<sup>2+</sup> are Jahn-Teller active and replacing Ni<sup>2+</sup> with the Jahn-Teller active Cu<sup>2+</sup> should result in a *c*-axis change. The change may be subtle since the local Jahn-Teller axis is not confined only to the *c* direction, and Cu<sup>2+</sup> is a larger ion regardless of the direction of Cu–O bond elongation/compression. The Shannon ionic radii of Ni<sup>2+</sup>, low-spin Ni<sup>3+</sup>, and Cu<sup>2+</sup> (all as 6-coordinate ions) are 0.69 Å, 0.56 Å, and 0.73

Å, respectively.  $^{42}$  The c/a ratio and unit cell volume are larger in Cu-NMC. It is known that Li<sup>+</sup> and Ni can partially substitute for each other in NMC.  $^{43}$  Furthermore, c/a ratios higher than 4.9 and the peak splits of the (006)/(012) and (018)/(110) reflections indicate a highly ordered layered structure.  $^{44}$  The extent of Wyckoff 3a/3b (Li/TM cation) mixing is assessed by the integrated peak ratio of  $I_{003}/I_{104}$ . Within the unit cell, the (003) plane is composed solely of Li-ion and the (104) plane is composed of *both* Li-ion and the TM ions (along with oxide anions as well;  $^{1/4}$  Li<sup>+</sup>, 1 TM,  $^{3/2}$  O<sup>2-</sup>). In a polycrystalline NMC sample with no Li/TM cation mixing, the calculated  $I_{003}/I_{104}$  ratio is 1.34. As the extent of Li/TM mixing increases,  $I_{003}/I_{104}$  decreases. Experimentally, the  $I_{003}/I_{104}$  ratios of NMC and Cu-NMC are 1.06 and 1.15, respectively, indicating that there is Li/TM cation mixing in both compounds, but that the extent of Li/TM cation mixing is smaller in Cu-NMC.

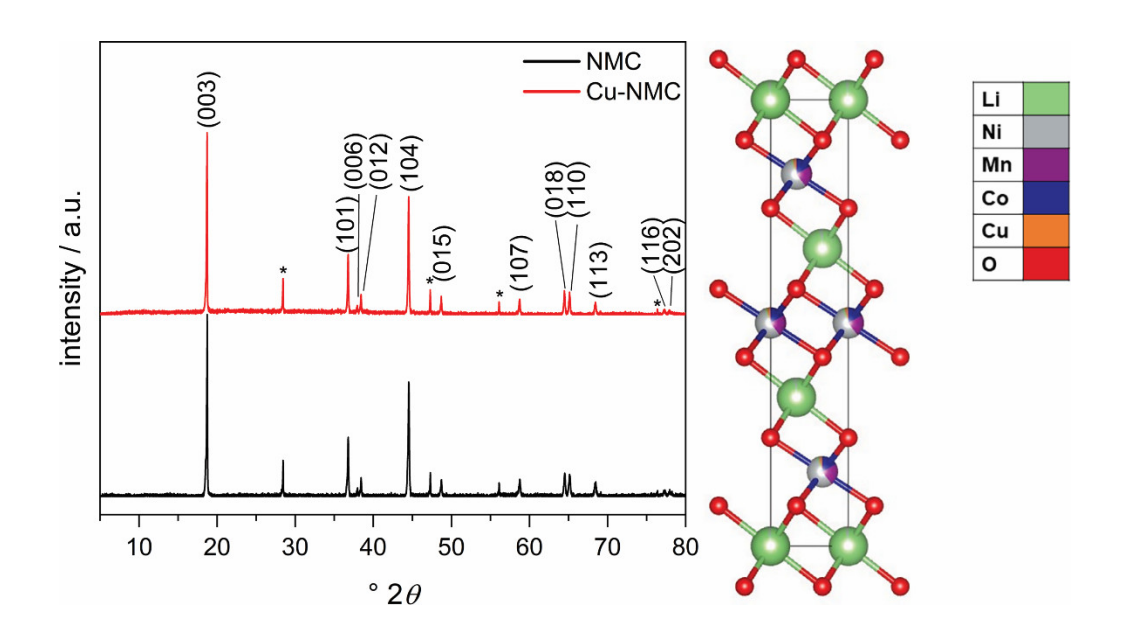


**Figure 1.** XRD patterns of NMC and Cu-NMC. Miller indices for NMC are provided and a Si standard of SRM 640e<sup>40</sup> denoted by (\*) was used to confirm peak positions.

The Rietveld refinement of the XRD data in **Figure 2** reveals these subtle differences, highlighted in **Table 1**: 1) NMC has a slightly smaller c-axis; the c/a ratio increases when  $Cu^{2+}$  is added; and 2) there is a small volumetric increase with added  $Cu^{2+}$ , both expected changes with the increased d-spacing for (003) and (104) Bragg planes. Also, these structural changes are consistent with a change in  $Ni^{3+}/Ni^{2+}$  ratio in doped Ni-rich materials,  $^{45,46}$  and motivates the combined structure/spectroscopy experiments that follow in this paper. In addition to hints at electronic structure changes, the Rietveld refinement also reveals a larger crystalline domain size ( $\tau$ ) and greater microstrain for 5 mol-% Cu-doped NMC, expected for greater lattice distortion

present in the doped material. We note that although these changes are small, they are statistically significant.

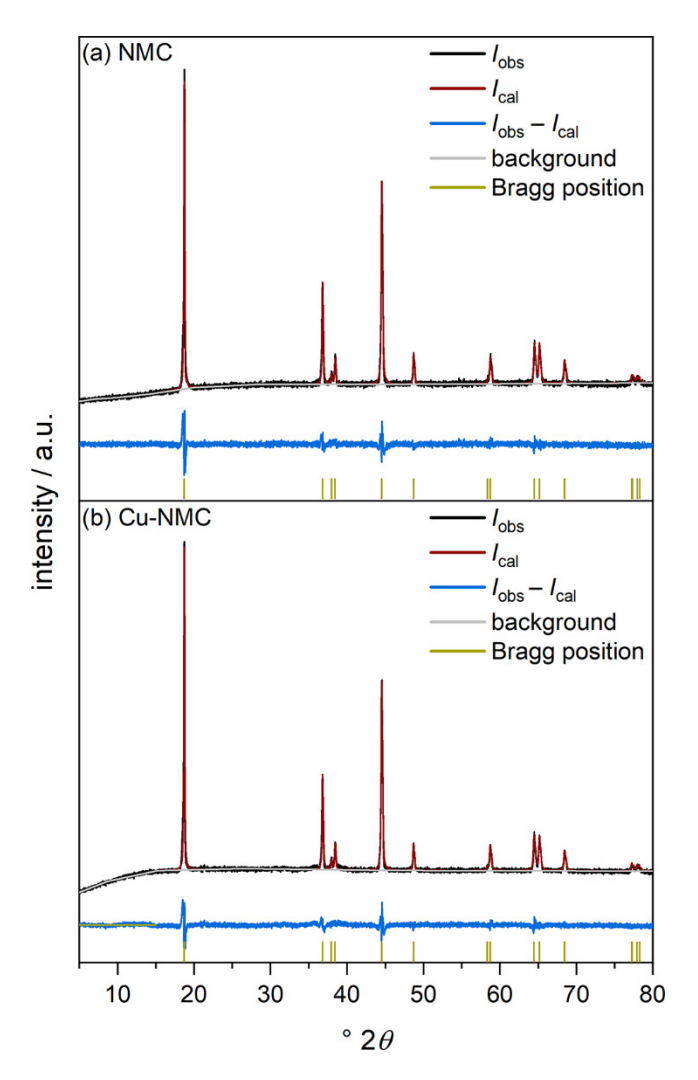
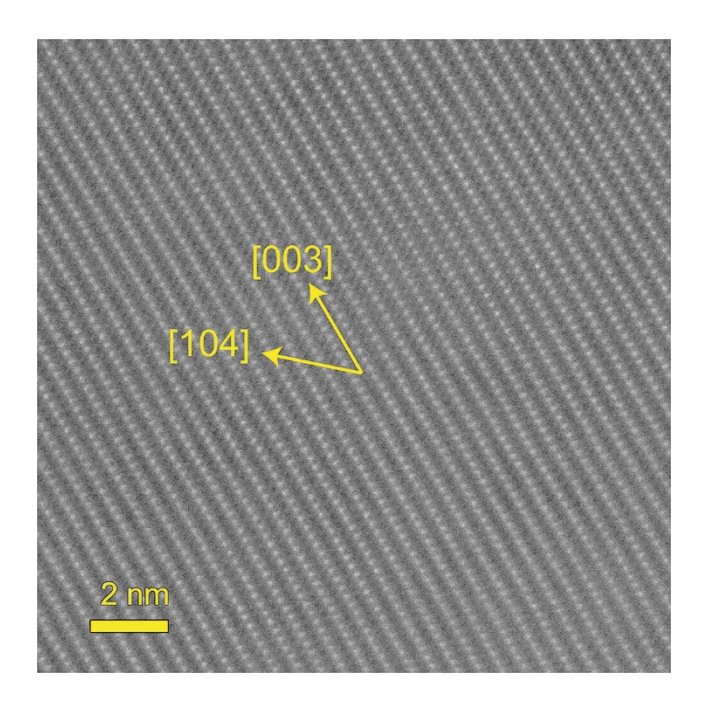


Figure 2. XRD pattern and Rietveld refinement of a) NMC and b) Cu-NMC.

**Table 1.** Crystal parameters obtained from Rietveld refinement of NMC and Cu-NMC.

Compound	a / Å	c / Å	c/a	$V/\mathrm{cm}^3$ $\mathrm{mol}^{-1}$	I003/104	τ / μm	Micro- strain	%wR	%R
NMC	2.86112	14.21166	4.9672	100.75	1.06	0.236	2273.4	3.32	2.20
Cu-NMC	2.86105	14.22284	4.9712	100.83	1.15	0.348	2697.8	3.10	2.04

SEM images and their associated EDX maps (**Figures S2** – **S3**) show a uniform distribution of the TM ions, according to the Grubbs outlier test, used to detect a single outlier in a univariate data set following an approximately normal distribution. A7,48 XRF elemental analysis data provide a stoichiometry of LiNi<sub>0.63</sub>Mn<sub>0.22</sub>Co<sub>0.15</sub>O<sub>2</sub> for the synthesized NMC622 and stoichiometry of LiNi<sub>0.56</sub>Mn<sub>0.22</sub>Co<sub>0.17</sub>Cu<sub>0.04</sub>O<sub>2</sub> for 5 mol-% Cu-NMC, which shows that Cu<sup>2+</sup> addition results in decreasing Ni-content. We note that doping is limited to 5 mol-%; when 10 mol-% Cu<sup>2+</sup> is added into the precursor reaction mixture, an impurity phase, Li<sub>2</sub>CuO<sub>2</sub>, appears (**Figure S4**). **Figure 3** shows the high-angle annular dark-field scanning transmission electron microscopy (HAADF-STEM) image of Cu-NMC used as an additional probe to the structural changes induced by Cu<sup>2+</sup> doping NMC. The image shows no evidence of copper localization in the Li layers or introduction of new grain boundaries, supporting the XRD refinement and lower degree of Li/TM cation mixing.



**Figure 3.** High-angle annular dark-field scanning transmission electron microscope (HAADF-STEM) of Cu-NMC viewed along the [110] zone axis, highlighting the [003] and [104] crystallographic directions.

Electrochemical Characterization. Figure 4 shows the CV trace of NMC and Cu-NMC. On the first scan starting from open circuit and sweeping to more positive potentials at a scan rate of 0.1 mV/s, NMC shows the expected anodic wave with a peak potential of 3.94 V and the corresponding reverse cathodic wave at 3.67 V, which is assigned to the formal Ni<sup>4+/2+</sup> couple and Co<sup>4+/3+</sup> couple. The Ni oxidation state slightly increases after each cycle as the Ni-based redox couple is not fully reversible; Ni redox chemistry accounts for ~67% of the battery capacity. On the other hand, the Co redox couple is fully reversible, and Co oxidation does not occur until ~3.8 V, while accounting for ~33% of the battery capacity. <sup>49,50</sup> Upon subsequent cycling, the NMC anodic peak shifts to more negative potential, 3.87 V, with virtually no shift in the corresponding cathodic peak. Adding 5 mol-% Cu<sup>2+</sup> shifts the anodic wave to a higher positive potential (beyond the 4.3 V switching potential) during the 1<sup>st</sup> cycle *and* shifts the cathodic wave to a more negative potential (3.54 V) relative to that observed for NMC. Upon subsequent CV scans, an anodic wave emerges within the scan window, with peak potential 4.05 V. This ~500 mV peak separation indicates larger overpotential for accessing the Ni<sup>4+/2+</sup> redox couple when 5 mol-% Cu<sup>2+</sup> is added.

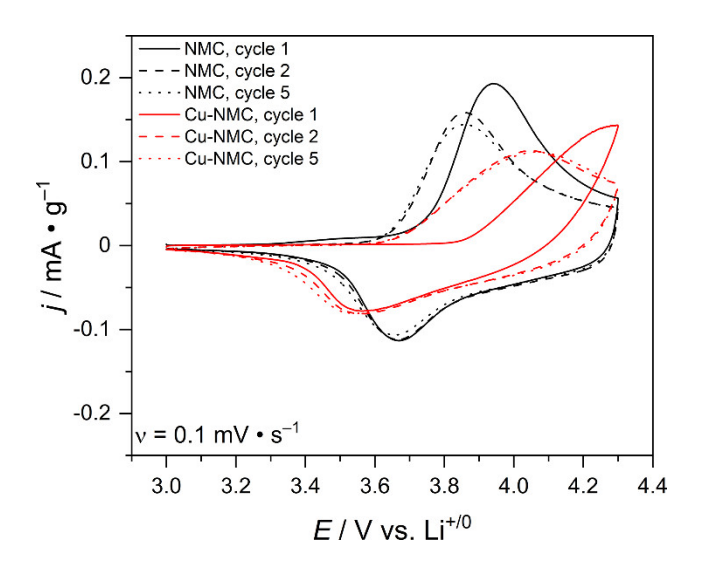


**Figure 4.** CV trace (IUPAC convention) from 3.0 - 4.3 V vs.  $Li^{+/0}$  sweeping in the positive direction starting at 3.0 V at 0.1 mV/s scan rate for NMC and Cu-doped NMC in half-cell coin cells.

Figure 5 shows the chronopotentiometry curves at 1 C current (175 mA/g) for NMC and Cu-NMC for the first cycle (i.e. - after assembling fresh cells and allowing them to rest for 6 h). NMC shows a relatively flat E - t charging profile with constant potential of ~3.8 V, consistent with 2-phase cycling, as has been reported. Cu-NMC requires greater potential to oxidize, indicating a delocalized electron model where there are distinct waves for Ni compared to Cu altering the potential at which Li inserts and extracts. This can be corroborated with **Figure 4** as there are shifts in the anodic and cathodic waves.

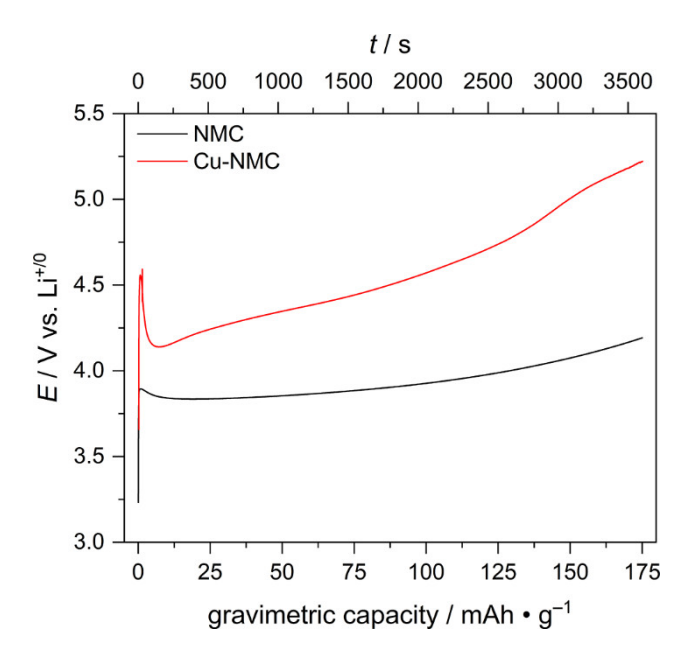


**Figure 5.** Chronopotentiometry (first charge at 1 *C* current) of NMC and Cu-NMC half-cell coin cells.

The potential vs. capacity plots (**Figure 6a, b**) and the discharge capacity plots (**Figure 6c, d**) show that the capacity increases initially from 197 mAh/g (0.81 mAh/cm²) in NMC to 216 mAh/g (0.91 mAh/cm²) in Cu-NMC, but during the higher 1 *C* current cycling, the specific discharge capacity drops to 102 mAh/g (0.43 mAh/cm²) for Cu-NMC compared to 136 mAh/g (0.58 mAh/cm²) for NMC. Cu-NMC does have less capacity fade as the specific discharge capacity is 91 mAh/g (0.38 mAh/cm²) after 100 cycles, compared to 96 mAh/g (0.39 mAh/cm²) for NMC. Also, when the discharge capacity retention is normalized to that observed for the 1<sup>st</sup> 1 *C* cycle, the capacity fade is only 11% after 97 cycles, compared to 30% for NMC. From previous studies, the Ni oxidation accounts for the majority of capacity and the Co<sup>4+/3+</sup> couple has been shown to be

reversible.<sup>50</sup> The overall drop in capacity is rationalized by replacing Ni sites with Cu<sup>2+</sup>, and the increased capacity retention is explained by the irreversible Ni redox couple accounting for less of the battery capacity during cycling in Cu-NMC. Moreover, with the increased crystalline domain size (Table 1) Li<sup>+</sup> diffusion becomes limiting at higher current. **Figure 7** shows that At higher current (0.5 *C*, 1 *C*, and 3 *C*), Cu-doping appears to slightly increase capacity, but at lower current (0.1 *C*, 0.2 *C*, and 0.3 *C*) NMC has higher capacity indicating that Cu-doping can be charged and discharged faster. Overall, both NMC and Cu-NMC recover well from the *C*-rate test by starting at 134 mAh/g (0.84 mAh/cm<sup>2</sup>) and 106 mAh/g (0.37 mAh/cm<sup>2</sup>) and ending at 120 mAh/g (0.75 mAh/cm<sup>2</sup>) and 107 mAh/g (0.37 mAh/cm<sup>2</sup>), respectively, for 0.1 *C* cycling.

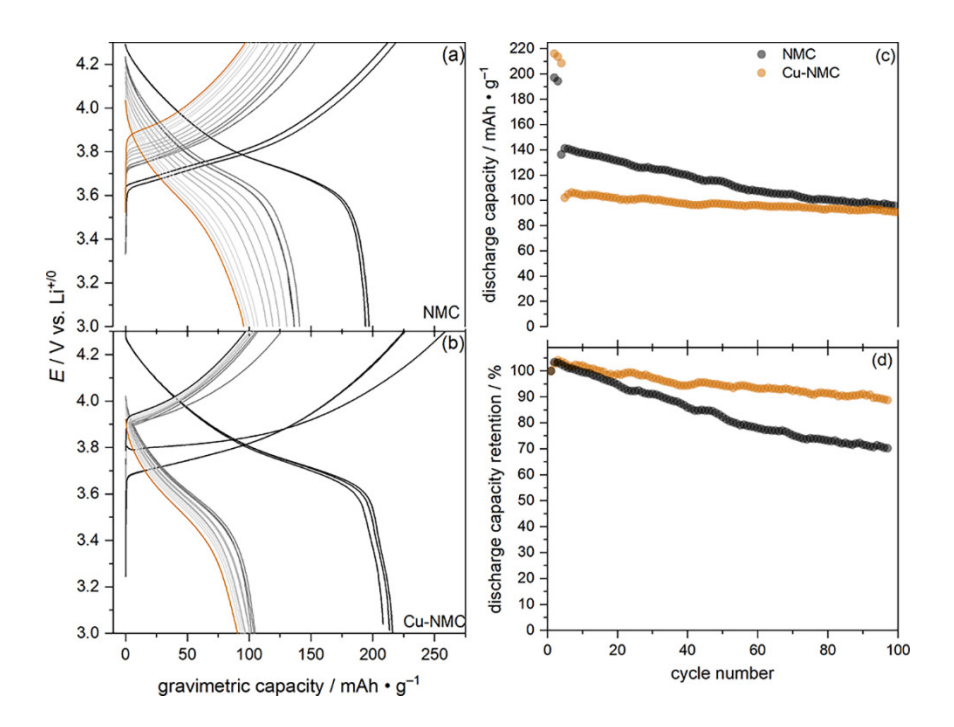


**Figure 6.** Potential vs. capacity plots of the three 0.1 *C* current formation cycles and the subsequent 97 1 *C* current cycles for (a) NMC and (b) Cu-NMC cycled in half-cell coin cells. Comparison of

NMC to Cu-NMC by (c) discharge capacity retention of 97 1 C cycles normalized to the 1st 1 C cycle and (d) specific discharge capacity of the cells cycled in half-cell coin cells from 3.0-4.3 V vs  $\text{Li}^{+/0}$ .

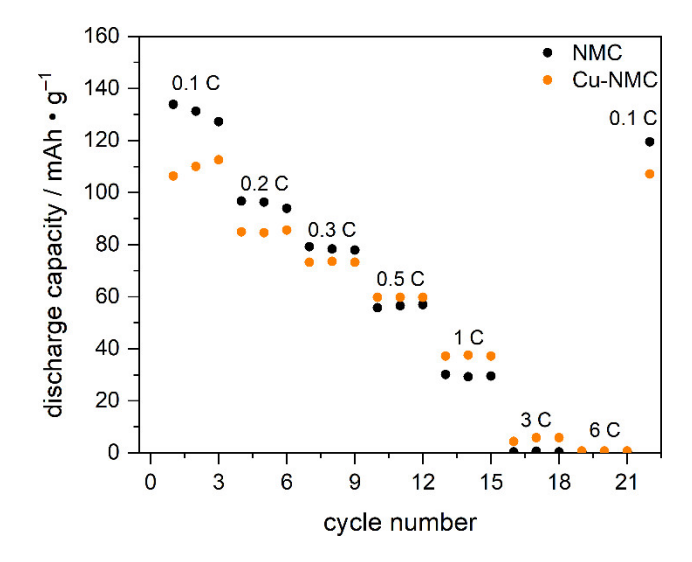


**Figure 7.** Specific discharge capacity at varying current (three cycles of 0.1 C, 0.2 C, 0.3 C, 0.5 C, 1 C, 3 C, and 6 C) of NMC and Cu-NMC cycled in half-cell coin cells from 3.0 – 4.3 V vs Li<sup>+/0</sup>.

Electrochemical impedance spectroscopy (EIS) data for Li-ion battery half-cells were modeled using a common two RC equivalent circuit model with a Warburg element.<sup>53</sup> The Nyquist plot in **Figure 8** (and corresponding Bode plots in **Figure S5a, b**) shows that when Cu<sup>2+</sup> is doped onto the 3b Wyckoff TM sites, the resistance associated with forming the SEI ( $R_{SEI}$ ) increases from 22  $\Omega$  to 310  $\Omega$  and the charge-transfer resistance ( $R_{ct}$ ) increases from 162  $\Omega$  to 1044  $\Omega$ . The larger  $R_{SEI}$  is observed in the first galvanostatic charge cycle of Figure 5 as more energy per unit charge is required to form the SEI in Cu-NMC indicated by the feature at ~30 s. Also, the resistance portion of Warburg impedance ( $W_R$ ) increases from 38  $\Omega$  for NMC to 4983  $\Omega$  for Cu-NMC with

a decrease in the slope (-1.37 - Z/Z) for Cu-NMC compared to NMC slope (-3.53 - Z/Z), showing that Cu-NMC is Li<sup>+</sup> diffusion limited. The full fitting parameters for this model are presented in **Table S1**. **Equation 3** provides the diffusion coefficient for Li ( $D_{Li}$ ), where  $V_m$  is the molar volume from Table 1, dE/dx is the slope from the coulometric titration (**Figure S5c**, **d**), F is Faraday's constant, A is the electrode area of 0.7854 cm<sup>2</sup>, and  $Z_w$  is the average Warburg element from frequency 100 Hz to 10 Hz (Figure S5b).<sup>54</sup> Cu-NMC shows slower diffusion kinetics ( $D_{Li} = 1.03 \times 10^{-10}$  cm<sup>3</sup>/mol) compared to NMC ( $D_{Li} = 7.91 \times 10^{-10}$  cm<sup>3</sup>/mol). We note that these diffusion coefficients are on the same order of magnitude as those previously reported Li-ion battery cathode materials, including NMC.<sup>55</sup>

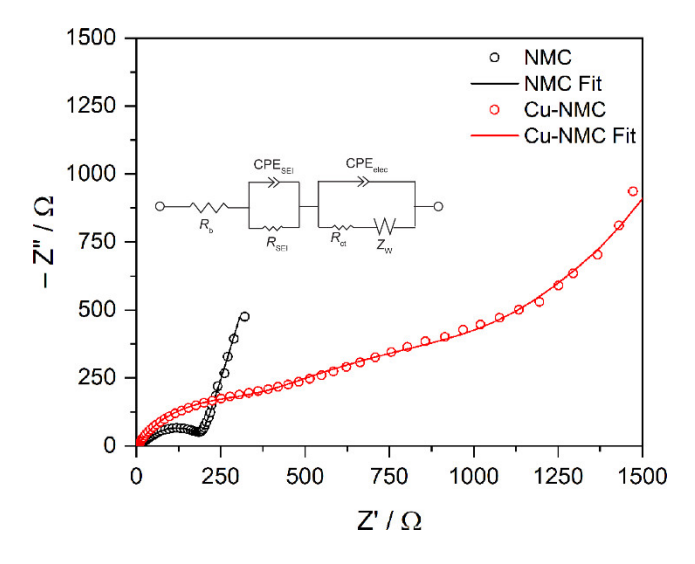


**Figure 8.** Nyquist plot of NMC and Cu-NMC EIS data with an amplitude of 10 mV and a frequency range of 100 KHz to 1 Hz. The equivalent circuit model is included in the inset.  $R_b$ : bulk resistance of the cell (electrolyte, separator, and electrodes),  $R_{SEI}$ , CPE<sub>SEI</sub>: resistance and

capacitance (modeled as a constant-phase element, CPE) of the interfacial layer,  $R_{ct}$ , and CPE<sub>elec</sub>: charge-transfer resistance and double-layer capacitance (modeled as a CPE), and W, Li<sup>+</sup> diffusion.

$$D_{Li} = \frac{\left(\frac{V_m \left(\frac{dE}{dx}\right)}{FAZ_W}\right)^2}{2} (3)$$

# Changes in Structure and Composition after Galvanostatic Cycling.

To assess how added Cu<sup>2+</sup> results in different behavior in galvanostatic cycling, we analyze XPS of Ni, specifically the  ${}^{2}P$  lines (Ni 2p core electrons) at varying states of charge. The XPS of the synthesized materials in **Figure 9** shows three features in the energy 845 – 890 eV energy range, a broad satellite peak and nickel present as both Ni<sup>3+</sup> and Ni<sup>2+</sup>. Integrating the higher binding energy  ${}^{2}P_{3/2}$  lines shows that the relative ratio of Ni<sup>3+</sup>:Ni<sup>2+</sup> on the surface increases from 1.56 in NMC to 1.89 in Cu-NMC. This increase in Ni<sup>3+</sup>:Ni<sup>2+</sup> ratio for Cu-NMC is consistent with aliovalent ion doping, which is corroborated by the XRD data. In the control experiment (Figure S6), the XPS for the TM hydroxide precursors resulting from the co-precipitation reaction in equation 1 shows much narrower <sup>2</sup>P lines with binding energies consistent only with Ni<sup>2+</sup>. In Figure S7, XPS of Cu, specifically the <sup>2</sup>P lines (Cu 2p core electrons) of Cu-NMC, confirms that Cu is in its 2+ formal oxidation, and the CV data in Figure 4 indicates no change in oxidation state for Cu during cycling. For the materials that have been cycled at constant current, the XPS of Cu-NMC shows a smaller increase in surface oxidation state Ni as the material is charged from 3.0 – 4.3 V (Figure 10 and Table 2). The smaller changes in Ni oxidation state ratio can account for the lower specific discharge capacity of the material, as there is less Ni<sup>2+</sup> to oxidize.

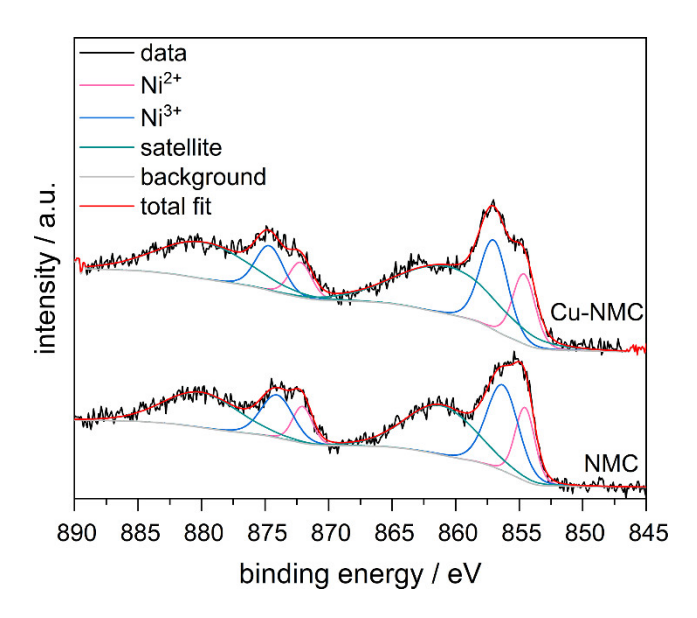
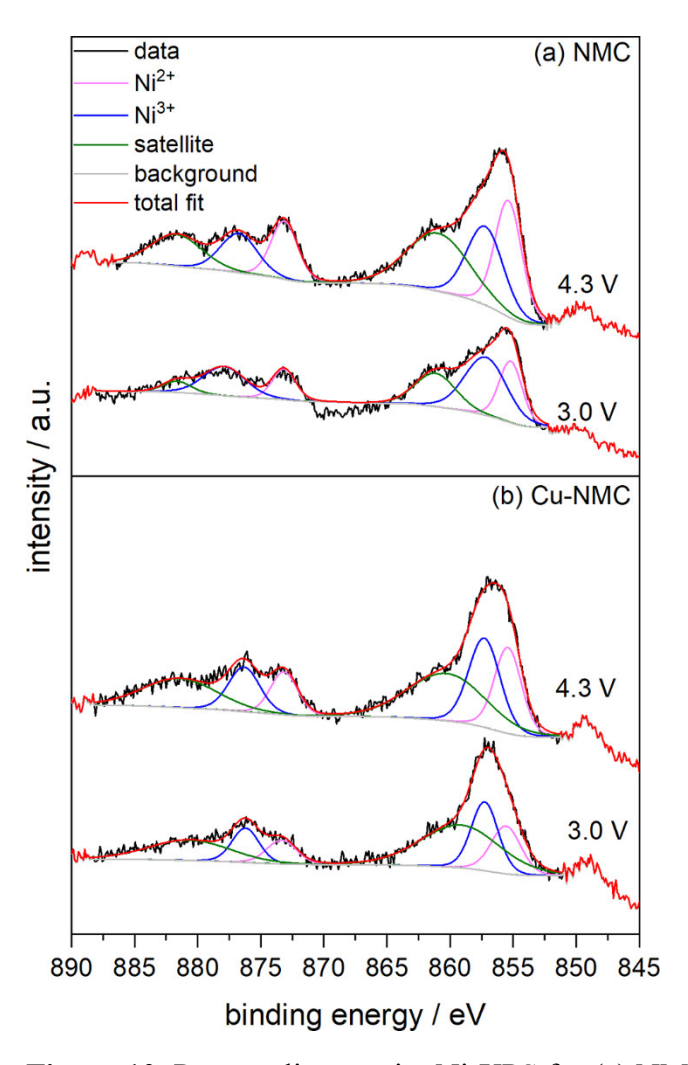


Figure 9. Ni-XPS spectra of synthesized NMC and Cu-NMC.



**Figure 10.** Post-cycling *ex*-situ Ni-XPS for (a) NMC and (b) Cu-NMC electrodes cycled in half-cell coin cells after formation cycles and charged at 1 C current to 3.0 V and 4.3 V vs. Li<sup>+/0</sup>.

**Table 2.** Ex-situ surface Ni oxidation state ratio of integrated XPS Ni  ${}^{2}P_{3/2}$  lines for electrodes cycled in half-cell coin cells after formation cycles and charged at 1 C current to 3.0 - 4.3 V.

Compound	3.0 V Ni <sup>3+</sup> :Ni <sup>2+</sup>	4.3 V Ni <sup>3+</sup> :Ni <sup>2+</sup>
NMC	0.59	1.09
Cu-NMC	0.77	0.83

At different states of charge, XRD is also measured to understand the changes in structure. As is shown in Figure S8a and b, there is an additional Bragg reflection at  $65.6^{\circ} 2\theta$ , at slightly higher angle than where the (110) reflection appears in the 4.3 V data. This new Bragg reflection represents the change from hexagonal phase 1 (H1) to hexagonal phase 2 (H2);<sup>56</sup> this H2(110) reflection indicates a change in the NMC layered structure at the top of charge. This structural change ultimately leads to a phase change to spinel, and the spinel gives rise to decrease in discharge capacity retention over time.<sup>57</sup> The presense of two (110) planes stems from the orientation created from mechanically pressing the electrode during cell assembly. Typically, the March-Dollase factor is used to account for texture (perfered orientation), and a single Bragg reflection internsity can be varried.<sup>58</sup> In this case, there are multiple reflections that change intensity, so a single factor is not valid. We scraped the electrode off of the current collector, and the XRD pattern from this experiment shows the H2 (110) plane disappear, illustrating the problem of assigning a second phase at the top of charge. Rather, the XRD patterns suggest a loss in prefered oreintation rather the presense of a true secondary phase. Table 3 presents the relevant parameters from XRD data collected from pre-cycled NMC and Cu-NMC electrode powders (Figure 11a and b) compared to the post-cycled electrode powders (**Figure 11c** and **d**). This is greater Li/TM cation mixing at the top of charge for NMC, while Cu-NMC shows lower Li/TM cation mixing than would be expected with any site substituion, meaning there is no Li in the TM 3b Wyckoff sites; rather Li vacancies occur only on the 3a Wyckoff sites. The domain size for NMC also decreases substantially (74.7%) at the top of charge indicating electrode pulverization that results in higher capacity fade. This pulverization is supported at the secondary particle level as well. SEM imaging in **Figure 12a** and **b** of the pre-cycled NMC and Cu-NMC electrode powders have particle sizes  $\sim 6~\mu m$  and 10  $\mu m$ , respectively. **Figure 12 c** and **d** show that after charging to 4.3 V, the particle size of NMC decreases to  $\sim 1.5~\mu m$  and Cu-NMC particles remain larger,  $\sim 5~\mu m$ . Cu-NMC has a larger volumetric change and lower change in microstrain, but the overall domain size decreases only by 40.5% at the top of charge acounting for the increased capacity retention. The smaller change in microstain and smaller change in domain size for Cu-NMC could have large impacts on solid-state batteries, as the maintaining both the macro- and microscale structures of the cathode mixture is critical for promoting ion transfer without fracture at the solid electrode-solid ionic conductor interface.  $^{59-61}$ 

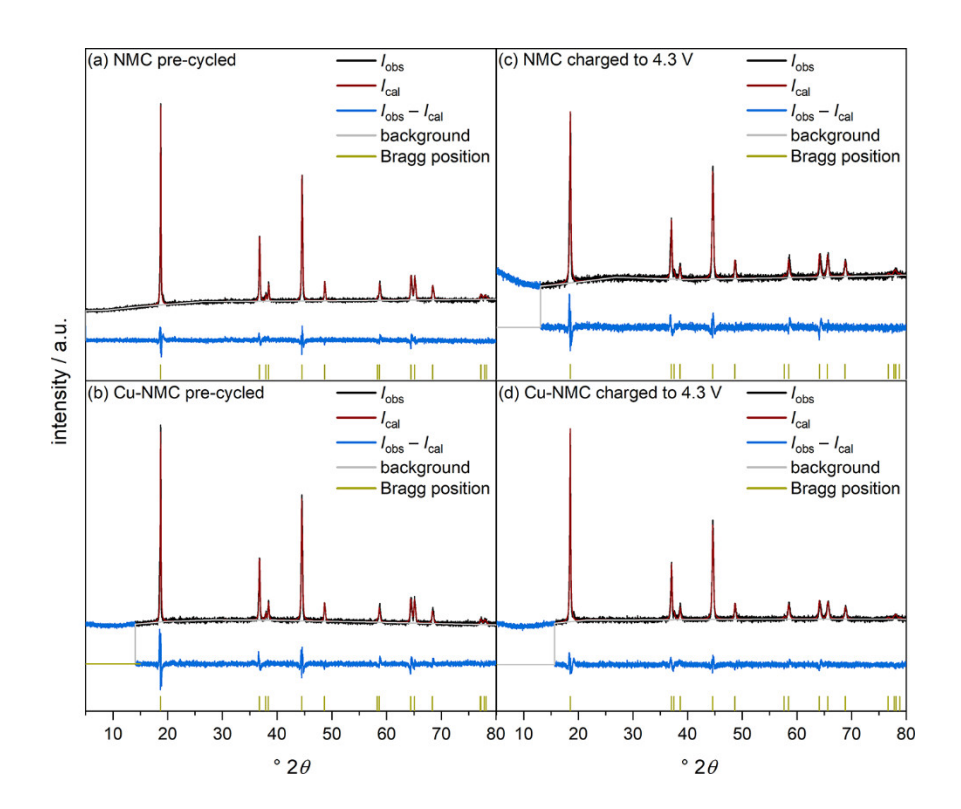


**Figure 11.** XRD Rietveld refinement of pre-cycled (a) NMC and (b) Cu-NMC electrode powders and post-cycling *ex-situ* XRD of (c) NMC and (d) Cu-NMC electrode powders cycled in half-cell coin cells after formation cycles and charged at 1 C current to 4.3 V vs. Li<sup>+/0</sup>.

Table 3. Crystal parameters obtained from Rietveld refinements of pre- and post-cycled NMC and Cu-NMC electrodes.

Compound	a / Å	c / Å	c/a	$V/\mathrm{cm}^3$ $\mathrm{mol}^{-1}$	$I_{003/104}$	$\tau/\ \mu m$	Micro-strain	%wR	%R
NMC Pre-Cycled	2.86206	14.22373	4.9698	100.9	1.12	0.2125	2466.2	3.19	2.34
NMC 4.3V	2.84407	14.36858	5.0521	100.7	1.30	0.0538	383.4	4.21	3.03
Cu-NMC Pre- Cycled	2.86419	14.2357	4.9702	101.1	1.15	0.1742	3008.9	4.16	2.68
Cu-NMC 4.3V	2.84243	14.37832	5.0584	100.6	1.42	0.1036	3634.3	3.06	2.35

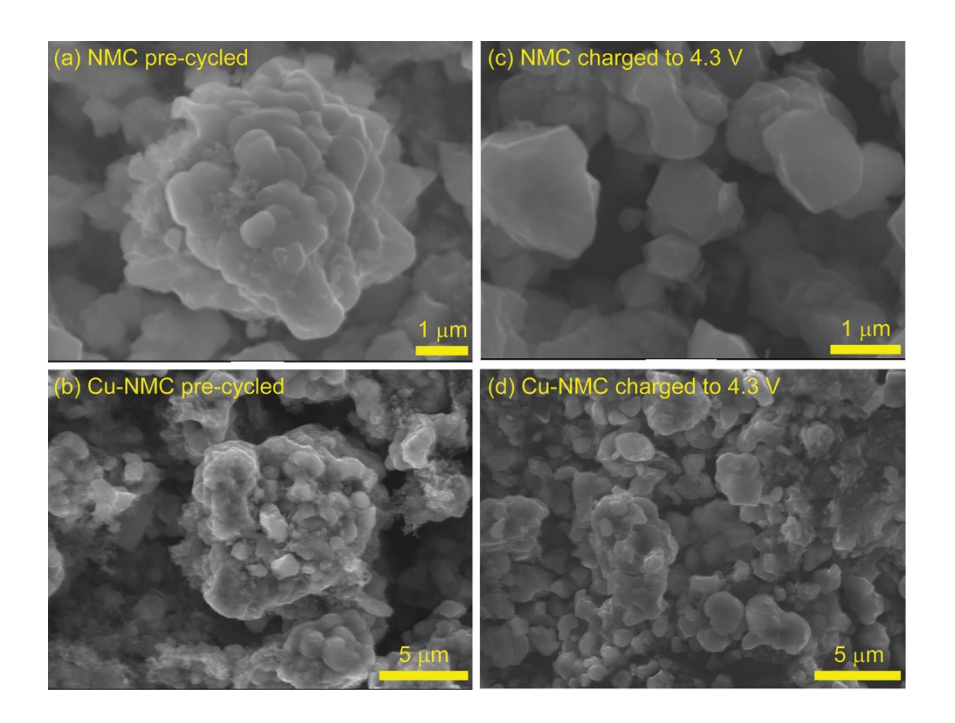


**Figure 12.** SEM images of pre-cycled (a) NMC and (b) Cu-NMC electrode powders and post-cycling images of (c) NMC and (d) Cu-NMC electrode powders cycled in half-cell coin cells after formation cycles and charged at 1 C current to 4.3 V vs. Li<sup>+/0</sup>.

# **Conclusions**

When doping NMC with Cu<sup>2+</sup> ion at 5 mol-%, phase pure *R*–3*m* layered material results, supported by XRF elemental analysis, XRD, and HAADF-STEM imaging. The degree of Li/TM cation mixing is smaller for Cu-NMC, and the unit cell volume is slightly larger as Jahn-Teller active Cu<sup>2+</sup> is added. Electrochemically, Cu<sup>2+</sup> doping gives rise to a decrease in capacity due to an increase in the oxidation state of Ni at the surface, illustrated by XPS. Cu<sup>2+</sup> also leads to an increase in both the resistance across the SEI layer as well as the charge-transfer resistance. Nevertheless,

the capacity retention in Cu-NMC is greater because the domain size decrease is smaller, leading to less pulverization of the particles upon repeated cycling. Future efforts in our group focus on

identifying new chemical compositions that mitigate particle fracture.

**Supporting Information** 

The Supporting Information is available free of charge at (web):

Additional XRD data, SEM images, EIS data and model for NMC and Cu-NMC; additional XPS

data

**AUTHOR INFORMATION** 

**Corresponding Author** 

\* e-mail: bartmb@umich.edu

**Author Contributions** 

The manuscript was written through contributions of all authors. All authors have given approval

to the final version of the manuscript.

Acknowledgements

This research was supported by the Mechano-chemical Understanding of Solid Ion Conductors,

an Energy Frontier Research Center funded by the U.S. Department of Energy, Office of Science,

Office of Basic Energy Science under grant no. DE-SC0023438. The authors also acknowledge

the financial support of the University of Michigan College of Engineering and NSF grant #DMR-

0420785, technical support from the Michigan Center for Materials Characterization, and technical

support from the Robert B. Mitchell Electron Microbeam Analysis Lab at the University of Michigan. The authors thank Drs. Allen Hunter and Tao Ma for preparing and imaging the STEM samples. The authors would also like to make a special acknowledgement to Dr. Geneva Laurita for help with performing Rietveld refinement.

#### References

- <sup>1</sup> McKerracher, C.; Izadi-Najafabadi, A.; Chatterton, R.; Kou, N., Albanese, N.; Soulopoulos, N.; Doherty, D.; Frith, J.; Grant, A.; Berryman, I.; Mi, S.; Asghar, A.; Abraham, T-C., Boers, M.; Commerford, J.; Zamorano-Cadavid, A. Fisher, R. *Electric Vehicle Outlook 2019*; BloombergNEF, New York, NY **2019**. https://legacy-assets.eenews.net/open\_files/assets/2019/05/15/document\_ew\_02.pdf. (accessed 2023-02-09)
- <sup>2</sup> Gupta, A.; Shukla, V. *Lithium-Ion Battery Market*; GMI/GMI1135; Global Market Insights, Selbyville, DE, 2023. https://www.gminsights.com/industry-analysis/lithium-ion-battery-market (accessed 2023-02-09)
- <sup>3</sup> Bak, S.; Hu, E.; Zhou, Y.; Yu, X.; Senanayake, S. D.; Cho, S.; Kim, K.; Chung, K. Y.; Yang, X.; Nam, K. Structural Changes and Thermal Stability of Charged LiNi<sub>x</sub>Mn<sub>y</sub>Co<sub>z</sub>O<sub>2</sub> Cathode Materials Studied by Combined In Situ Time-Resolved XRD and Mass Spectroscopy. *ACS Appl. Mater. Iterfaces.* **2014**, *24* (6), 22594-22601. DOI: 10.1021/am506712c
- <sup>4</sup> Jin, D.; Park, C.; Han, J.; Dzakpasu, C. B.; Kim, E.; Oh, J.; Kim, K. M.; Lee, S.; Lee, Y. M. Ethyl 2-(2-fluoroethoxy)ethyl carbonate as a new electrolyte additive for high-voltage Li-metal batteries. *Battery Energy.* **2023**, *2* (1), 1-11, DOI: 10.1002/bte2.20220034
- <sup>5</sup> Jung, R.; Metzger, M.; Maglia, F.; Stinner, C.; Gasteiger, H. A.; Oxygen Release and Its Effect on the Cycling Stability of LiNi<sub>x</sub>Mn<sub>y</sub>Co<sub>z</sub>O<sub>2</sub> (NMC) Cathode Materials for Li-Ion Batteries. *J. Electrochem Soc.* **2017**, *164* (7), A1361-A1377 DOI: 10.1149/2.0021707jes
- <sup>6</sup> Quilty, C. D.; Bock, D. C.; Yan, Y.; Takeuchi, K. J.; Takeuchi, E. S.; Marschilok, A. C. Probing Sources of Capacity Fade in LiNi<sub>0.6</sub>Mn<sub>0.2</sub>Co<sub>0.2</sub>O<sub>2</sub> (NMC622): An *Operando* XRD Study of Li/NMC622 Batteries during Extended Cycling. *J. Phys. Chem. C.* **2020**, *124*, 8119-8128. DOI: 10.1021/acs.jpcc.0c00262
- <sup>7</sup> Jung, R.; Linsenmann, F.; Thomas, R.; Wandt, J.; Solchenbach, S.; Maglia, F.; Stinner, C.; Tromp, M.; Gasteiger, H. A. Nickel, Manganese, and Cobalt Dissolution from Ni-Rich NMC and

- Their Effects on NMC622-Graphite Cells. *J. Electrochem. Soc.* **2019**, *166*, A378-A389. DOI: 10.1149/2.1151902jes
- <sup>8</sup> Leng, Y.; Ge, S.; Marple, D.; Yang, X.; Bauer, C.; Lamp, P.; Wang, C. Electrochemical Cycle-Life Characterization of High Energy Lithium-Ion Cells with Thick Li(Ni<sub>0.6</sub>Mn<sub>0.2</sub>Co<sub>0.2</sub>)O<sub>2</sub> and Graphite Electrodes. *J. Electrochem. Soc.* **2017**, *164*, A1037-A1049 DOI: 10.1149/2.0451706jes
- <sup>9</sup> Wang, X.; Ding, Y.; Deng. Y.; Chen. Z. Ni-Rich/Co-Poor Layered Cathode for Automotive Li-Ion Batteries: Promises and Challenges. *Adv. Energy Mater.* **2020**, *10*, 1903864. DOI: 10.1002/aenm.201903864
- <sup>10</sup> Gujarathi, P. K.; Shah, V. A.; Lokhande, M. M. Cost Analysis for Conversion of Conventional Vehicle into Plug-In Hybrid Electric Vehicle. *J. Green Engineering.* **2018**, *4*, 497-518. DOI: 10.13052/jge1904-4720.843
- <sup>11</sup> Reynaud, M.; Serrano-Sevillano, J.; Casas-Cabanas, M. Imperfect Battery Materials: A Closer Look at the Role of Defects in Electrochemical Performance. *Chem. Mater.* **2023**, *35* (9), 3345-3363. DOI: 10.1021/acs.chemmater.2c03481
- <sup>12</sup> Wu, J.; Zhang, X.; Ju, Z.; Wang, L.; Hui, Z.; Mayilvahanan, K.; Takeuchi, K. J.; Marschilok, A. C.; West, A. C.; Takeuchi, E. S.; Yu, G. From Fundamental Understanding to Engineering Design of High-Performance Thick Electrodes for Scalable Energy-Storage Systems. *Adv. Mater.* **2021**, 33, 2101275. DOI: 10.1002/adma.202101275
- <sup>13</sup> Yu, Y.; Karayaylali, P.; Giordano, L.; Crchado-Gracía, J.; Hwang, J.; Sokaras, D.; Maglia, F.; Jung, R.; Gittleson, F. S.; Shao-Horn, Y. Probing Depth-Dependent Transition-Metal Redox of Lithium Nickel, Manganese, and Cobalt Oxides in Li-Ion Batteries. *ACS Appl. Mater. Interfaces.* **2020**, *12*, 55865-55875. DOI: 10.1021/acsami.0c16285
- <sup>14</sup> Philip, N. D.; Westover, A. S.; Daniel, C.; Veith, G. M. Structural Degradation of High Voltage Lithium Nickel Manganese Cobalt Oxide (NMC) Cathodes in Solid-State Batteries and Implications for Next Generation Energy Storage. *ACS Appl. Energy Mater.* **2020**, *3*, 1768-1774. DOI: 10.1021/acsaem.9b02230
- <sup>15</sup> Johnson, C. S.; Li, N.; Lefief, C.; Vaughey, J. T.; Thackeray, M. M. Synthesis, Characterization and Electrochemistry of Lithium Battery Electrodes: xLi<sub>2</sub>MnO<sub>3</sub>·(1 x)LiMn<sub>0.333</sub>Ni<sub>0.333</sub>Co<sub>0.333</sub>O<sub>2</sub> (0 ≤ x ≤ 0.7) *Chem. Mater.* **2008**, *20*, 6095–6106. DOI: 10.1021/cm801245r
- <sup>16</sup> Nation, L.; Wu, Y.; James, C.; Qi, Y.; Powell, B. R.; Sheldon, B. W. Si-doped high-energy Li<sub>1.2</sub>Mn<sub>0.54</sub>Ni<sub>0.13</sub>Co<sub>0.13</sub>O<sub>2</sub> cathode with improved capacity for lithium-ion batteries. *J. Mater. Res.* **2018**, *33*, 4182-4191. DOI: 10.1557/jmr.2018.378
- <sup>17</sup> Hashem, A.M.; Abdel-Ghany, A.E.; Scheuermann, M.; Indris, S.; Ehrenberg, H.; Mauger, A.; Julien, C.M. Doped Nanoscale NMC333 as Cathode Materials for Li-Ion Batteries. *Materials* **2019**, *12*, 2899. DOI: 10.3390/ma12182899

- <sup>18</sup> Zhang, R.; Wang, C.; Zou, P.; Lin, R.; Ma, L.; Yin, L.; Li, T.; Xu, W.; Jia, H.; Li, Q.; Sainio, S.; Kisslinger, K.; Trask, S. E.; Ehrlich, S. N.; Yang, Y.; Kiss, A. M.; Ge, M.; Polzin, B. J.; Lee, S. J.; Xu, W.; Ren, Y.; Xin, H. L. Compositionally complex doping for zero-strain zero-cobalt layered cathodes. *Nature*. **2022**, *610*, 67–73. DOI:10.1038/s41586-022-05115-z
- <sup>19</sup> Wang, L.; Sun, Y.; Hu, L.; Piao, J.; Guo, J.; Manthiram, A.; Ma, J.; Cao, A.; Copper-substituted Na<sub>0.67</sub>Ni<sub>0.3-x</sub>Cu<sub>x</sub>Mn<sub>0.7</sub>O<sub>2</sub> cathode materials for sodium-ion batteries with suppressed P2–O2 phase transition. *J. Mater. Chem. A.* **2017**, 5, 8752-8761. DOI: 10.1039/C7TA00880E
- <sup>20</sup> Wang, K.; Zhuo, H.; Wang, J.; Poon, F.; Sun, X.; Xiao, B. Recent Advances in Mn-Rich Layered Materials for Sodium-Ion Batteries. *Adv. Funct. Mater.* **2023**, *33*, 2212607. DOI: 10.1002/adfm.202212607
- <sup>21</sup> Wang, K.; Yan, P.; Wang, Z.; Fu, J.; Zhang, Z.; Ke, X.; Sui, M. Advancing layered cathode material's cycling stability from uniform doping to non-uniform doping. *J. Mater. Chem. A.* **2020**, *8*, 16690-16697. DOI: 10.1039/D0TA05262K
- <sup>22</sup> Pimlott, J. L.; Street, R. J.; Down, M. P.; Banks, C. E. Electrochemical Overview: A Summary of ACo<sub>x</sub>Mn<sub>y</sub>Ni<sub>z</sub>O<sub>2</sub> and Metal Oxides as Versatile Cathode Materials for Metal-Ion Batteries. *Adv. Funct. Mater.* **2021**, 31, 2107761. DOI: 10.1002/adfm.202107761
- <sup>23</sup> Gaines, L.; Wnag, Y. How to Maximize the Value Recovered from Li-Ion Batteries: Hydrometallurgical or Direct Recycling?. *Electrochem. Soc. Interface.* **2021**, *30* (3), 51-54. DOI: 10.1149/2.F07213F
- <sup>24</sup> Jacoby, M. It's time to get serious about recycling lithium-ion batteries. c&en (Northfield, II), July 14, 2019, updated July 14, 2019. https://cen.acs.org/materials/energy-storage/time-serious-recycling-lithium/97/i28 (accessed 2023-02-09)
- <sup>25</sup> Gratz, E.; Sa, Q.; Aoelian, D.; Wnag, Y. A closed loop process for recycling spent lithium ion batteries. *J. Power Sources.* **2014**, *262*, 255-262. DOI: 10.1016/j.jpowsour.2014.03.126
- Wang, J.; Chen, T. Surface composition and electrochemical behavior of LiNi1/3Co1/3Mn1/3O2 cathode material with copper additive. *Rare Met. (Beijing, China)*. **2012**, 31 (4), 397-401. DOI: 10.1007/s12598-012-0527-2
- <sup>27</sup> Sa, Q.; Heelan, J. A.; Lu, Y.; Apelian, D.; Wang, Y. Copper Impurity Effects on LiNi1/3Mn1/3Co1/3O2 Cathode Material. *ACS Appl. Mater. Interfaces.* **2015**, *7*, 20585–20590. DOI: 10.1021/acsami.5b04426
- <sup>28</sup> Zhang, R.; Meng, Z.; Ma, X.; Chen, M.; Chen, B.; Zheng, Y.; Yao, Z.; Vanaphuti, P.; Bong, S.; Yang, Z.; Wang, Y. Understanding fundamental effects of Cu impurity in different forms for recovered LiNi<sub>0.6</sub>Co<sub>0.2</sub>Mn<sub>0.2</sub>O<sub>2</sub> cathode materials. *Nano Energy.* **2020**, *78*, 105214 DOI: 10.1016/j.nanoen.2020.105214
- <sup>29</sup> Marks, T.; Trussler, S.; Smith, A. J.; Xiong, D.; Dahn J.R. A Guide to Li-Ion Coin-Cell Electrode Making for Academic Researchers. *J. Electrochem. Soc.* **2011**, *158*, A51-A57. DOI: 10.1149/1.3515072

- <sup>30</sup> Hao, X.; Gourdon, O.; Liddle. B. J.; Bartlett, B. M. Improved electrode kinetics in lithium manganospinel nanoparticles synthesized by hydrothermal methods: identifying and eliminating oxygen vacancies. *J. Mater. Chem.* **2012**, *22*, 1578-1591, DOI: 10.1039/C1JM15583K
- <sup>31</sup> Scribner Associates Release 2019-2: ZView; Scribner Associates, Inc: North Carolina, 2019. https://www.scribner.com/software/68-general-electrochemistr376-zview-for-windows/
- <sup>32</sup> Materials Data Release 2005-7: Jade6.5.26; Materials Data, Inc; California, 2005. https://www.materialsdata.com/index.html#Products (accessed 2023)
- <sup>33</sup> Hashem, A. M.; El-Tawil, R.S.; Abutabl, M.; Eid, A. E. Pristine and coated LiNi<sub>1/3</sub>Mn<sub>1/3</sub>Co<sub>1/3</sub>O<sub>2</sub> as positive electrode materials for li-ion batteries. *Res. Eng. Struct. Mat.* **2015**, *1*, 81-97. DOI: 10.17515/resm2015.07en0315
- <sup>34</sup> Toby, B. H.; Von Dreele, R. B. *GSAS-II*: the genesis of a modern open-source all purpose crystallography software package *J. Appl. Cryst.* **2013**, *46*, 544-549. DOI: 10.1107/S0021889813003531
- <sup>35</sup> SRM 660c; *LaB*<sub>6</sub>; National Institute of Standards and Technology; U.S. Department of Commerce: Gaithersburg, MD (19 December 2023).
- <sup>36</sup> Rietveld, H. M. A profile refinement method for nuclear and magnetic structures. *J. Appl. Cryst.* **1969**, *2*, 65-71. DOI: J. Appl. Cryst. (1969). 2, 65-71. DOI: 10.1107/S0021889869006558
- <sup>37</sup> Momma, K.; Izumi, F. VESTA 3 for three-dimensional visualization of crystal, volumetric and morphology data. *J. Appl. Crystallogr.* **2011**, *44*, 1272-1276. DOI: 10.1107/S0021889811038970
- <sup>38</sup> Fairley, N.; Fernandez, V.; Richard-Plouet, M.; Guillot-Deudon, C.; Walton, John; Smith, E.; Flahaut, D.; Greiner, M.; Biesinger, M.; Tougaard, S.; Morgan, D.; Baltrusaitis, J. Systematic and collaborative approach to problem solving using X-ray photoelectron spectroscopy. *Applied Surface Science Advances.* **2021**, *5*, 100112. DOI: 10.1016/j.apsadv.2021.100112
- <sup>39</sup> Entwistle, T.; Sanchez-Perez, E.; Murray, G. J.; Anthonisamy, N.; Cussen, S. A. Coprecipitation synthesis of nickel-rich cathodes for Li-ion batteries. *Energy Rep.* **2022**, *8*, 67 73. DOI: 10.1016/j.egyr.2022.06.110
- <sup>40</sup> SRM 640e; *Silicon*; National Institute of Standards and Technology; U.S. Department of Commerce: Gaithersburg, MD (19 December 2023).
- <sup>41</sup> Sun, H.; Zhao, K. Electronic Structure and Comparative Properties of LiNi<sub>x</sub>Mn<sub>y</sub>Co<sub>z</sub>O<sub>2</sub> Cathode Materials. *J. Phys. Chem. C.* **2017**, *121*, 6002-6010. DOI: 10.1021/acs.jpcc.7b00810
- <sup>42</sup> Shannon, R.D. Revised Effective Ionic Radii and Systematic Studies of Interatomic Distances in Halides and Chalcogenides. *Acta Cryst.* **1976**, *A32*, 751-767. DOI: 10.1107/S0567739476001551

- <sup>43</sup> Yin, L.; Li, Z.; Mattei, G. S.; Zheng, J.; Zhao, W.; Omenya, F.; Fang, C.; Li, W.; Li, J.; Xie, Q.; Erickson, E. M.; Zhang, J.; Whittingham, M. S.; Meng, Y. S.; Manthiram, A. Thermodynamics of Antisite Defects in Layered NMC Cathodes: Systematic Insights from High-Precision Powder Diffraction Analyses. *Chem. Mater.* **2020**, 32, 3, 1002–1010. DOI: 10.1021/acs.chemmater.9b03646
- <sup>44</sup> Peng, G.: Yao, X.; Wan, H.; Huang, B.; Yin, J.; Ding, F.; Xu, X. Insights on the fundamental lithium storage behavior of all-solid-state lithium batteries containing the LiNi<sub>0.8</sub>Co<sub>0.15</sub>Al<sub>0.05</sub>O<sub>2</sub> cathode and sulfide electrolyte. *J. Power Sources.* **2016**, 307, 724-730. DOI: 10.1016/j.jpowsour.2016.01.039
- <sup>45</sup> Kosova, N. V.; Devyatkina, E. T.; Kaichev. V. V.; Optimization of Ni<sup>2+/</sup>Ni<sup>3+</sup> ratio in layered Li(Ni,Mn,Co)O<sub>2</sub> cathodes for better electrochemistry. *J. Power Sources.* **2007**, 174, 965-969. DOI: 10.1016/j.jpowsour.2007.06.051
- <sup>46</sup> Hua, W.; Zhang, J.; Zheng, Z.; Liu, W.; Peng, X.; Guo, X.; Zhong, B.; Wang, Y.; Wang, X. Nadoped Ni-rich LiNi<sub>0.5</sub>Co<sub>0.2</sub>Mn0.3O<sub>2</sub> cathode material with both high rate capability and high tap density for lithium ion batteries. *Dalton Trans.* **2014**, *43*, 14824-14832. DOI: 10.1039/C4DT01611D
- <sup>47</sup> Grubbs, F. Procedures for Detecting Outlying Observations in Samples. *Technometrics* **1969**, 11, 1-21.
- <sup>48</sup> Harris, D. C. Statistics. In *Quantitative Chemical Analysis*, 9th ed.; W. H, Freeman and Company, 2016; pp 65-94.
- <sup>49</sup> Liang, L.; Sun. X.; Wu. C.; Hou, L.; Sun, J.; Zhang, X.; Yuan, C. Nasicon-Type Surface Functional Modification in Core–Shell LiNi<sub>0.5</sub>Mn<sub>0.3</sub>Co<sub>0.2</sub>O<sub>2</sub>@NaTi<sub>2</sub>(PO<sub>4</sub>)<sub>3</sub> Cathode Enhances Its High-Voltage Cycling Stability and Rate Capacity toward Li-Ion Batteries. *ACS Appl. Mater. Interfaces.* **2018**, *10*, 5498-5510. DOI: 10.1021/acsami.7b15808
- <sup>50</sup> Tallman, K. R.; Wheeler, G. P.; Kern, C. J.; Stavitshi, E.; Tong, X.; Takeuchi, K. J.; Marschilok, A. C.; Bock, D. C.; Takeuchi, E. S. Nickel-rich Nickel Manganese Cobalt (NMC622) Cathode Lithiation Mechanism and Extended Cycling Effects Using Operando X-ray Absorption Spectroscopy. *J. Phys. Chem. C* **2021**, 125, 1, 58–73. DOI: 10.1021/acs.jpcc.0c08095
- <sup>51</sup> Li, J.; Shumugasundaram, S.; Doig, R.; Dahn J. R. In Situ X-ray Diffraction Study of Layered Li–Ni–Mn–Co Oxides: Effect of Particle Size and Structural Stability of Core–Shell Materials. *Chem. Mater.* **2016**, 28, 162-171. DOI: 10.1021/acs.chemmater.5b03500
- <sup>52</sup> Wang, X.; Fan, X.; Yu, X.; Bak, S.; Shadike, Z.; Waluyo, I.; Hunt. A.; Senanayake, S. D.; Li, H.; Chen, L.; Wang, C.; Xiao, R.; Hu, E.; Yang, X. The Role of Electron Localization in Covalency and Electrochemical Properties of Lithium-Ion Battery Cathode Materials. *Adv. Funct. Mater.* **2021**, 31, 2001633. DOI: 10.1002/adfm.202001633

- <sup>53</sup> Choi, W.; Shin, H.; Kim, M. J.; Choi, J.; Yoon, W. Modeling and Applications of Electrochemical Impedance Spectroscopy (EIS) for Lithium-ion Batteries. *J. Electrochem. Sci. Technol.* **2020**, *11*, 1-13. DOI: 10.33961/jecst.2019.00528
- <sup>54</sup> Hao, X.; Gourdon, O.; Liddle, B.; Bartlett, B. M. Improved electrode kinetics in lithium manganospinel nanoparticles synthesized by hydrothermal methods: identifying and eliminating oxygen vacancies. *J. Mater. Chem.* **2012**, 22, 1578-1591. DOI: 10.1039/C1JM15583K
- <sup>55</sup> Ashton, T. E.; Baker, P. J.; Sotelo-Vazquez, C.; Footer, C. J. M.; Kojima, K. M.; Matsukawa, T.; Kamiyama, T.; Darr, J. A. Stoichiometrically driven disorder and local diffusion in NMC cathodes. *J. Mater. Chem A.* **2021**, 9, 10477-10486. DOI: 10.1039/D1TA01639C
- <sup>56</sup> Wang, X.; Zhou, H.; Chen, Z.; Meng, X. Synchrotron-based X-ray diffraction and absorption spectroscopy studies on layered LiNi<sub>x</sub>Mn<sub>y</sub>Co<sub>z</sub>O<sub>2</sub> cathode materials: A review. *Energy Storage Mater.* **2022**, 49, 181-208. DOI: 10.1016/j.ensm.2022.04.012
- <sup>57</sup> Quilt, C. D.; Wheeler, G. P.; Wang, L.; McCarthy, A. H.; Yan, S.; Tallman, K. R.; Dunkin, M. R.; Tong, X.; Ehrlich, S.; M. L.; Takeuchi, K. J.; Takeuchi, E. S.; Bock, D. C.; Marschilok, A. C. Impact of Charge Voltage on Factors Influencing Capacity Fade in Layered NMC622: Multimodal X-ray and Electrochemical Characterization. *ACS Appl. Mater. Interfaces* **2021**, 13, 43, 50920–50935. DOI: 10.1021/acsami.1c14272
- <sup>58</sup> Dollase, W.A. Correction of Intensities for Preferred Orientation in Powder Diffractometry: Application of the March Model. *J. Appl. Crystallogr.* **1986**, *19*, 267 272. DOI: 10.1107/S0021889886089458
- <sup>59</sup> Zhang, X.; Yue, F.; Liang, J.; Li, H.; Guo, Y. Structure Design of Cathode Electrodes for Solid-State Batteries: Challenges and Progress. *Small Struct.* **2020**, 1, 2000042. DOI: 10.1002/sstr.202000042
- <sup>60</sup> Wu, J.; Shen, L.; Zhang, Z.; Liu, G.; Wang, Z.; Zhou, D.; Wan, H.; Xu, X.; Yao, X. All-Solid-State Lithium Batteries with Sulfide Electrolytes and Oxide Cathodes. *Electrochem. Energ. Rev.* **2021**, 4, 101-135. DOI: 10.1007/s41918-020-00081-4
- <sup>61</sup> Yang, J.; Huang, B.; Yin, J.; Yao, X.; Peng, G.; Zhou, J.; Xu, X. Structure Integrity Endowed by a Ti-Containing Surface Layer towards Ultrastable LiNi<sub>0.8</sub>Co<sub>0.15</sub>Al<sub>0.05</sub>O<sub>2</sub> for All-Solid-State Lithium Batteries. *J. Electrochem. Soc.* **2016**, 163, A1530. DOI: 10.1149/2.0331608jes

# TOC Graphic

